DOI: 10.13009/EUCASS2019-536

DOI: ADD DOINUMBER HERE

Strategies for high performance GNSS/IMU Guidance, Navigation and Control of Rocketry

Pablo Solano-López[⋆,†,‡], *Raúl de Celis*[⋆,†], *Manuel Fuentes*[⋆,‡], *Luis Cadarso*[⋆] *and Adrián Barea*[⋆]
[⋆]*European Institute for Aviation Training and Accreditation (EIATA), Universidad Rey Juan Carlos*
Camino del Molino S/N 28943, Fuenlabrada, Madrid, Spain.
[‡]*Universidad Politécnica de Madrid*
Plaza del Cardenal Cisneros, 3, 28040 Madrid, Spain
pablo.solano@urjc.es · raul.decelis@urjc.es
[†]Corresponding author

Abstract

Although Artillery rockets suffered a lack of accuracy in its aiming, proportional to its range, the introduction of GNSS and Inertial sensors allowed to overcome this problematic. Nevertheless, some issues remained due to its highly non-linear dynamics (fast spinning, inertia coupling), causing errors on attitude and position determination during terminal stages. We propose in this paper the addition of a low-cost sensor (quadrant photo-detector) and a hybridization of its information with the former ones, so this terminal guidance is achieved satisfactory. These results are tested over a rocket realistic flight model that is validated and fully detailed in the paper.

1. Introduction

Weapon design and development have always identify two important parameters throughout its history: Precision and cost, and artillery rockets are no exception to that. Indeed, one of the great advantages of a precise missile is minimizing the so-called 'collateral damage'. Also, without such precise weapons, the viability of the use of force or continued military action would become unacceptable.[6]

We can define a precision-guided munition (PGM) as a guided missile that is conceived to precisely hit a specific target, minimizing collateral damage. The guidance of the PGM is usally performed by means of two main inputs: The reception of positioning from Global Navigation Satellite Systems (GNSS) and the outputs from Inertial navigation systems.

Position, velocity, and timing signals from GNSS, such as the Global Positioning System (GPS), are used throughout the world. However, their availability and reliability has become a subject of concern for all kind of applications. In order to defend against jamming, independent sources of navigation information are needed. For example, attenuation of the GNSS signal can be caused by trees, buildings, or antenna orientation, and result in reduced signal/noise ratio even without interference. This loss of signal can result in an increase in effective jammer/signal level even without intentional jamming or interference.

Inertial navigation systems, on the other hand, cannot be jammed. The major error sources in the inertial navigation system are due to gyro and accelerometer inertial sensor imperfections, incorrect navigation system initialization, and imperfections in the gravity model used in the computations. Therefore, they are an excellent source of navigation information to be integrated with GNSS receivers.[3]

A part from precision, cost is an important design variable, and in some cases the increase on accuracy can be achieved also by reducing the cost of the rocket by taking advantage of the available technology. An interesting manner to achieve that is to substitute the receivers by lower-cost sensors and then integrate or hybridize their outputs. The benefits of integrated data fusion have been demonstrated across the spectrum of antisubmarine, tactical air, and land warfare.[14] Also, advantages and issues for different types of INS augmented with GNSS updates have been studied by many authors[12].[11] When other sensors are available, they may be additional inputs to a filter, more commonly, the Kalman filter.

Indeed, GNSS/IMU hybridizing systems provide accurate solutions for PGMs but in some occasions these solutions might not be enough. For those systems, a Circle Error Probable (CEP) is around 10-20 m in the best cases.[3] Similarly to,[3] there have been previous research on stability and controllability of these types of systems. In order to

DOI: 10.13009/EUCASS2019-536

design control systems,[1] state that the governing equations of motion are accurately modeled by taking into account the effect of the mass rate and the center of gravity shift and linear time invariant (LTI) models are obtained by linearizing them at specific operating points.[4] detail the design and simulation of an attitude guidance and control scheme for a spinning aerospace vehicle. Two single-input/single-output controllers are used, which in turn issue flap deflection commands.[9] noticed that the stable region of the design parameters for the autopilot shrinks significantly under the spinning condition. They also observed that the stable region for design parameters is further narrowed when an integrator is introduced into the acceleration loop while the steady-state accuracy is dramatically improved. The control law is specifically formulated to rely on feedback only from a strap-down detector and roll angle sensors.[8] propose a discrete-time, proportional-derivative navigation guidance law for the terminal phase of an engagement with emphasis on the effect of a digital implementation.[13] present a complete design concerning the guidance and autopilot modules for a class of spin-stabilized fin-controlled projectiles. The proposed concept is composed of two sections: the rapidly spinning aft part contains the charge, whereas the front part, which is roll decoupled from the aft.

Note that in typical GNSS/IMU integrated navigation systems, there exist unknown disturbances and abnormal measurements, which are of key importance during terminal guidance. For example,[5] present a novel image-based guidance and control algorithm for small-diameter spin-stabilized projectiles. Therefore, development of algorithms for low-cost high-precision terminal guidance systems is a cornerstone in research on PGMs during the following years.

In addition to the aforementioned GNSS/IMU sensors, modern weapons include laser guidance capability, offering high precision, all-weather attack capability.[2] An example of theses systems can be seen on,[10] where they design a missile target tracker using a filter/correlator based on forward-looking infrared sensor measurements. Indeed, Semi Active Laser kits (SAL), and particularly quadrant detector devices, have been developed in order to improve precision in guided weapons. These quadrant photo-detectors are common in many engineering applications, such as measurement, control, laser collimation, target tracking, and particularly in our case of study: PGM terminal guidance.[7] One of the greatest advantages of quadrant detector equipment is the high performance provided in terms of guidance, typically in the last stages of the trajectory, as compared to the low cost incurred. Except for a requirement of line of sight verification and the allocation of codes prior to the mission, the use of SAL does not impose further limitations or complexities when operating in good visibility conditions, (day or night) and therefore it is suitable for ad-hoc engagements of targets of opportunity and close air support.

The aim of this paper is to improve the existing methods for terminal guidance applying a simple but effective hybridization algorithm in order to obtain the desired measurements from a combination of sensors previously mentioned to be applied on a guidance, navigation and control system. It is organized as follows. In Section II the system modeling is described in detail. Section III describes navigation, guidance and control algorithms. Section IV shows simulations results. Finally, discussion and conclusions follow.

2. System Modeling

Throughout this section the rocket, the control actuactor and the employed sensors will be described, together with their non-linear flight dynamics model.

2.1 Rocket

The guidance and control formulation proposed in this study applies to a 140 mm axisymmetric spinning rocket with wrap around stabilizing fins. It features supersonic launch speed and a spin rate of approximately 150 Hz. The maneuver mechanism is operated with a roll-decoupled fuse placed at the nose of the rocket. This fuse is composed of four canard surfaces, decoupled 2 by 2, in order to generate desired control force modulus and argument, oriented in an orthogonal plane relative to rocket, and its associated moment as it is exposed in Figure 1.

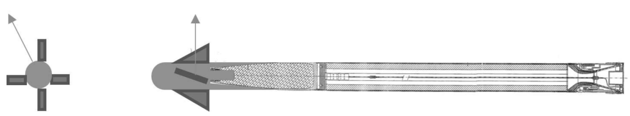

Figure 1: 140 mm axisymmetric spinning rocket with wrap around fins, decoupled 2 by 2, a roll-decoupled fuse and its actuation force.

Rocket parameters are shown in Table 1. The non-controlled solid propellant thrust curve is shown in Figure 2. Equation 1 reproduces rocket mass variation versus time. Numerical simulations were developed in order to obtain aerodynamic coefficients for the rocket under study. Their values versus Mach number are shown in Figure 3.

DOI: 10.13009/EUCASS2019-536

$$m(t) = m_0 - \int_{t=0}^{t=t_b} \frac{T(\tau)}{F_t I_{sp}} d\tau, \tag{1}$$

$m(t)$ is the rocket mass function of time, m_0 is rocket initial mass, $T(t)$ is thrust modulus, which is also function of time, F_t is an experimental correction factor and Isp is the specific impulse of propellant.

Parameter	Maximum thrust	Burn-out time	Initial mass	Propellant mass	I_{x0}	I_{y0}	X_{CG0}	Caliber
Value	29160.00 N	2.70 s	62.40 kg	21.00 kg	0.19 kgm^2	18.85 kgm^2	1.13 m	0.14 m

Table 1: 140 mm axisymmetric spinning rocket main parameters.

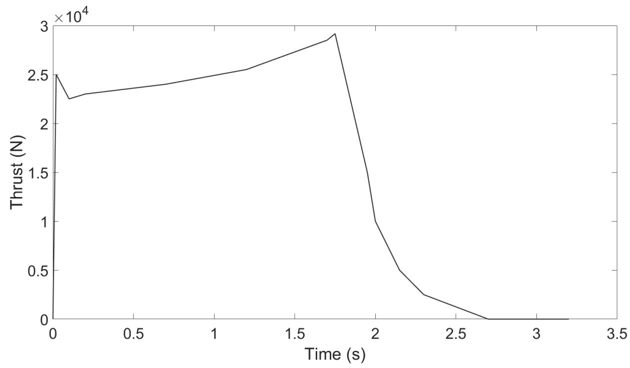

Figure 2: Thrust curve versus time.

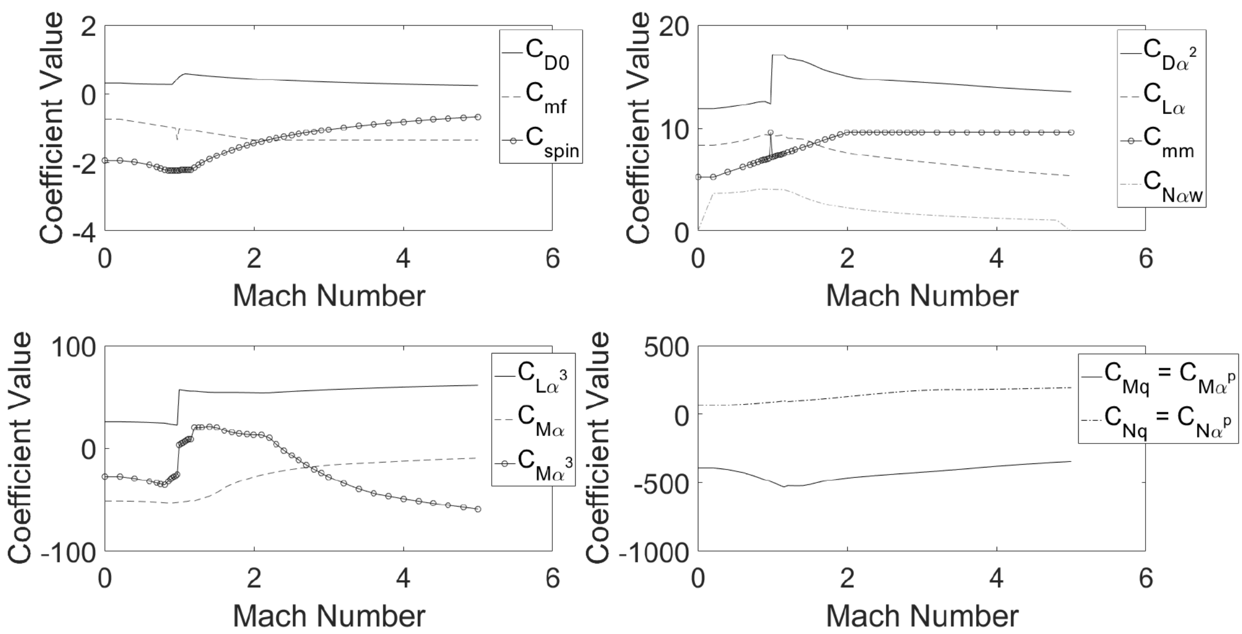

Figure 3: Rocket aerodynamic coefficients versus Mach number.

2.2 Flight Dynamics Model

Three axes systems are defined in order to express forces and moments: earth axes, body axes, and working axes. Earth axes are defined by sub index e. x_e pointing north, z_e perpendicular to x_e and pointing nadir, and y_e forming a clockwise trihedron. Working axes are defined by sub index w. x_w pointing to the target, y_w perpendicular to x_w and pointing

DOI: 10.13009/EUCASS2019-536

zenith, and z_w forming a clockwise trihedron. AZ_0 is the angle between x_e and x_w , in other words, the initial azimuth. Body axes are defined by sub index b. x_b pointing forward and contained in the plane of symmetry of the rocket, z_b perpendicular to x_b pointing down and contained in the plane of symmetry of the rocket, and y_b forming a clockwise trihedron. The origin of body axes is located at the center of mass of the rocket and they are severely coupled to the roll-decoupled fuse. Earth, body and working axes systems are illustrated in Figure 4.

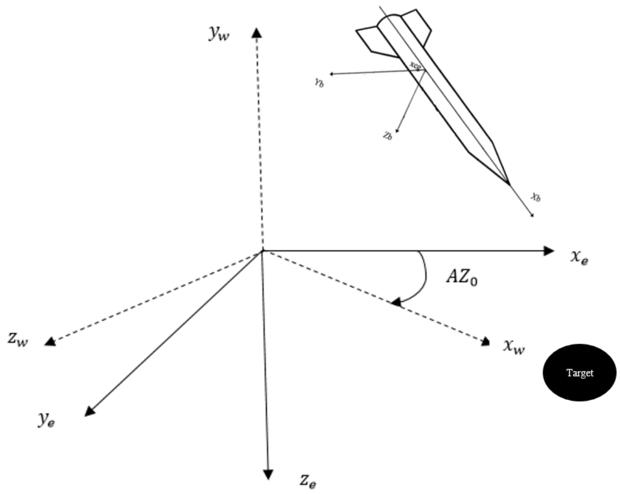

Figure 4: Reference systems.

The flight dynamics model in[3] is employed to model flight performance. In order to solve the motion of the rocket body reference frame, which is coupled to the fuse, is used. Because, the fuse is uncoupled from the rear part, which spins at high rates, it is required to model spinning motion to account for rear Magnus force and moment, and gyroscopic effects. It is assumed that the fuse mass is negligible, which implies that non-appreciable reactions are involved between fuse and aft part. Taking this into account, the aft effect is expressed as an extra addition of external forces and moments to the Newton-Euler equations expressed in the b reference system as it is demonstrated in.[3] The equations of motion are integrated forward in time using a fixed time step Runge-Kutta scheme of fourth order to obtain a single flight trajectory.

The result for a non-controlled trajectory, i.e., a ballistic trajectory, calculated by this model is shown in Figure 5 for initial pitch angles (θ_0) of 20, 30 and 45 degrees.

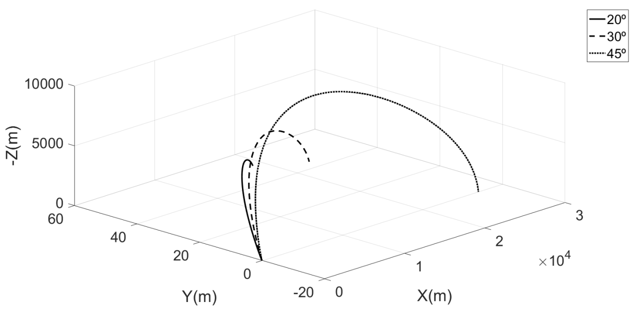

Figure 5: Ballistic trajectories for initial pitch angles (θ_0) of 20, 30 and 45 degrees.

Actuator Model

In order to model the control forces and moments in body axes for each of the four fins, we must consider first the effective incidence aerodynamic speed on each of the four fins. Figure 6 shows decomposition of incidence aerodynamic speed on a single fin. Note that lateral component of aerodynamic speed on the fin is neglected.

The mathematical expressions for this incidence aerodynamic speed decomposition are defined in 2 and 3:

$$\overrightarrow{v_{eff_{x_i}}} = \vec{v_b} - (\vec{v_b} \cdot \overrightarrow{u_{b_i}})\overrightarrow{u_{b_i}} \qquad \forall i \in \{1, 2, 3, 4\}, \tag{2}$$

DOI: 10.13009/EUCASS2019-536

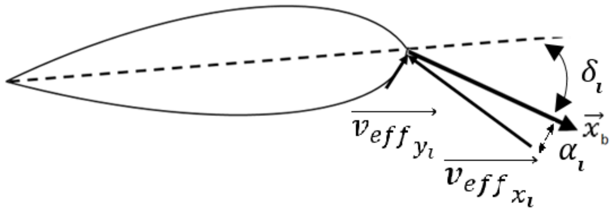

Figure 6: Incidence aerodynamic speed decomposition, local angle of attack (α_i), and fin deflection (δ_i).

$$\overrightarrow{v_{eff_{y_i}}} = \vec{v_b} - (\vec{v_b} \cdot \overrightarrow{u_{b_i}})\overrightarrow{u_{b_i}} - ((\vec{v_b} - (\vec{v_b} \cdot \overrightarrow{u_{b_i}})\overrightarrow{u_{b_i}}) \cdot \vec{x_b})\vec{x_b} \qquad \forall i \in \{1, 2, 3, 4\}, \tag{3}$$

where i denotes the fin, $\overrightarrow{v_{eff_{x_i}}}$ and $\overrightarrow{v_{eff_{y_i}}}$ are the aerodynamic speed minus the fin-span component of the aerodynamic speed and the perpendicular component of $\overrightarrow{v_{eff_{x_i}}}$ to x_b, respectively, $(\vec{v_b})$, $\overrightarrow{u_{b_1}} = [0, 0, -1]$, $\overrightarrow{u_{b_2}} = [0, -1, 0]$, $\overrightarrow{u_{b_3}} = [0, 0, 1]$, and $\overrightarrow{u_{b_4}} = [0, 1, 0]$.

The effective angle of attack for each fin (α_{eff_i}) may be expressed for each fin as the sum of the local angle of attack, α_i, and fin deflection, δ_i (see 4):

$$\alpha_{eff_i} = \alpha_i + \delta_i = sign(\overrightarrow{v_{eff_{y_i}}} \cdot \overrightarrow{u_{FN_i}})acos\left\{\frac{\overrightarrow{v_{eff_{x_i}}}}{||\overrightarrow{v_{eff_{x_i}}}||} \cdot \vec{x_b}\right\} + \delta_i \qquad \forall i \in \{1, 2, 3, 4\}, \tag{4}$$

where $\overrightarrow{u_{FN_1}} = [0, 1, 0]$, $\overrightarrow{u_{FN_2}} = [0, 0, -1]$, $\overrightarrow{u_{FN_3}} = [0, -1, 0]$, and $\overrightarrow{u_{FN_4}} = [0, 0, 1]$.

And finally the control force provided by each fin ($\overrightarrow{CF_i}$) is given in equation 5:

$$\begin{aligned}\overrightarrow{CF_i} = \tfrac{1}{8} sign(\alpha_{eff_i}) d^2 \rho\pi ||\overrightarrow{v_{eff_{x_i}}}||^2 (C_{N\alpha_w} cos(\alpha_{eff_i}) + \\ + \tfrac{2}{d^2\pi} S_{exp} sin^2(\alpha_{eff_i}))(\overrightarrow{u_{FN_i}} cos\delta_i - \vec{x_b} sin\delta_i),\end{aligned} \tag{5}$$

where d is the rocket caliber, ρ is the air density, $C_{N\alpha_w}$ is the aerodynamic coefficient of the normal force for a fin and S_{exp} is the characteristic surface of airfoil.

The total control force ($\overrightarrow{CF}$) is expressed in 6.

$$\overrightarrow{CF} = \sum_{i=1}^{i=4} \overrightarrow{CF_i} \tag{6}$$

The control moment provided by each fin ($\overrightarrow{CM_i}$) may be expressed as in 7:

$$\overrightarrow{CM_i} = (d_{ax}(M)\vec{x_b} + d_{lat}\overrightarrow{u_{b_i}}) \times \overrightarrow{CF_i}, \tag{7}$$

where $d_{ax}(M)$ is the longitudinal distance, parallel to x_b, of airfoil center of pressure (CP) to rocket center of mass (CG), which depends on Mach number (M). d_{lat} is the lateral distance, which is orthogonal to x_b and parallel to u_{b_i} for each fin, from airfoil center of pressure to rocket center of mass; it is supposed to be constant in this model. These distances are illustrated in Figure 7.

The total control moment ($\overrightarrow{CM}$) is given in 8.

$$\overrightarrow{CM} = \sum_{i=1}^{i=4} \overrightarrow{CM_i} \tag{8}$$

2.3 Sensors

In this paper, a hybridized GNSS/IMU system and Semi-active laser kit signals are fused in order to improve projectile performance in terms of accuracy.

The GNSS/IMU system is modeled as a random noise and a bias added to the model calculated position and attitudes. It is not the objective of this paper to model a GNSS/IMU hybridized system. Note that these hybridized systems have typical accuracies of 1 m and angular errors of 0.1 degrees; therefore, random noise and bias parameters have

DOI: 10.13009/EUCASS2019-536

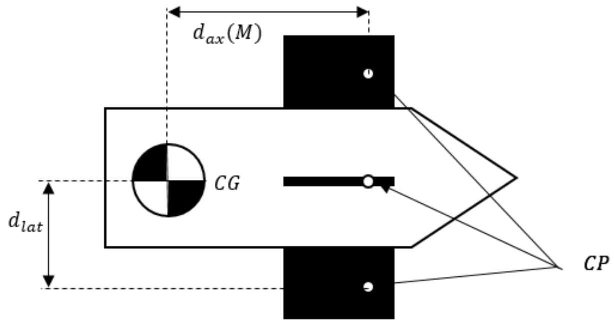

Figure 7: $d_{ax}(M)$ and d_{lat} scheme.

been adjusted to satisfy these characteristics. This accuracy permits good performance for intermediate trajectories. The expression that represents the vector between rocket and target or line of sight ($\overrightarrow{X_{p_{wGNSS/IMU}}}$) is shown in 9.

$$\overrightarrow{X_{p_{wGNSS/IMU}}} = [x_{w_{T_{GNSS/IMU}}} - x_{w_{R_{GNSS/IMU}}}, \\ , y_{w_{T_{GNSS/IMU}}} - y_{w_{R_{GNSS/IMU}}}, z_{w_{T_{GNSS/IMU}}} - z_{w_{R_{GNSS/IMU}}}], \tag{9}$$

where $[x_{w_{T_{GNSS/IMU}}}, y_{w_{T_{GNSS/IMU}}}, z_{w_{T_{GNSS/IMU}}}]$ is the position in working axes of the target, meassured by GNSS/IMU system, and $[x_{w_{R_{GNSS/IMU}}}, y_{w_{R_{GNSS/IMU}}}, z_{w_{R_{GNSS/IMU}}}]$ is the position of rocket center of gravity at each instant expressed in working axes, measured by GNSS/IMU system with its associated error.

During final stages of flight, errors of 1 m in positioning target and rocket induces enormous errors on rocket center of mass and target vector as it is demonstrated in the following sections. Therefore an accurate terminal guidance sensor such as a semi-active laser quadrant photo detector is recommended for these final flight stages. This semi-active laser sensor, combined with GNSS/IMU data, will provide an accurate determination of the vector between rocket center of mass and target, which is essential for navigation algorithms employed during this paper.

Semi-active laser kit consists of a quadrant photo detector that may be modeled as in Figure 8,[2] where the outer circle models the detector and the inner one the laser spot. In order to estimate laser footprint spot center coordinates, electric intensities provided by each of the photo diodes (I_1, I_2, I_3 and I_4), which depend on the area illuminated by the laser spot, may be used. The most suitable algorithm is defined by equations 10,[2] where $[x_{quad}, y_{quad}]$ are the calculated laser footprint spot center coordinates.

$$\left\{ \begin{array}{c} x_{quad} \\ y_{quad} \end{array} \right\} = \left\{ \begin{array}{c} ln\frac{I_4}{I_2} \\ ln\frac{I_1}{I_3} \end{array} \right\} \tag{10}$$

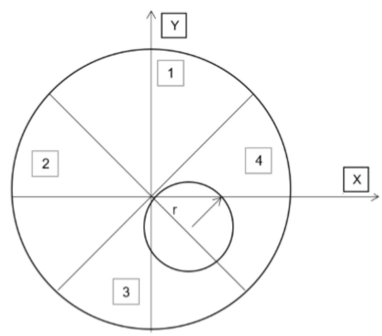

Figure 8: Quadrant photo-detector configuration used.

Relationship between $y_c/x_c = y_{quad}/x_{quad}$ is kept, i.e., the transformation is conformal as indicated in equation 11, where x_c and y_c are the real spot center positions, not positions obtained by 10. Radial measurements may be interpolated using as interpolation points the following Table 2,[2] where real and measured radial distances, r_c and r_{quad}, respectively, are defined in equations 12 and 13:

DOI: 10.13009/EUCASS2019-536

r_{quad}	0.48	0.99	1.50	2.01	2.67	3.68	5.88
r_c	0.1	0.2	0.3	0.4	0.5	0.6	0.7

Table 2: Interpolation between measured radial distance, r_{quad}, and real radial distance, r_c.

$$\theta_c = \theta_{quad} = atan\frac{y_{quad}}{x_{quad}} \tag{11}$$

$$r_{quad} = \sqrt{x_{quad}^2 + y_{quad}^2} \tag{12}$$

$$r_c = f(r_{quad}) \tag{13}$$

Then, the measurement output of the quadrant detector sensor may be expressed as it is indicated in 14, where R_{quad} is the physical radius of the quadrant detector:

$$\left\{ \begin{array}{c} x_c \\ y_c \end{array} \right\} = R_{quad} \left\{ \begin{array}{c} r_c cos\theta_c \\ r_c sin\theta_c \end{array} \right\} \tag{14}$$

For a single quadrant detector, the unitary line of sight vector expressed in body axes shall respond to the following expression 15, where d_{pCG} is the distance from the quadrant detector to the center of mass of the rocket:

$$\overrightarrow{X_{p_b}} = \frac{[d_{pCG}, x_c, y_c]}{\sqrt{d_{pCG}^2 + x_c^2 + y_c^2}} \tag{15}$$

3. Navigation, Guidance and Control

This section describes in detail the proposed navigation, guidance and control algorithms.

3.1 Navigation

Navigation for this system refers to the determination, during the totality of flight, of the rocket position and target position, i.e., the relationship between rocket center of mass and target positions, which is called line of sight, and rocket attitude. Line of sight can be obtained on earth axes by subtracting rocket position, determined by GNSS/IMU sensors from target position, but as it was previously explained, this method induces enormous errors on final stages of flight as it is shown in Figure 9.

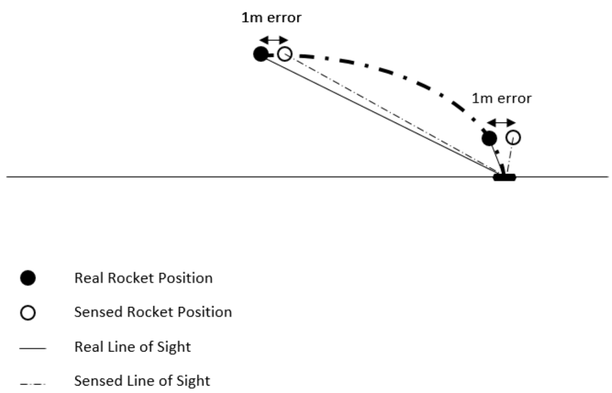

Figure 9: Errors on line of sight determination by GNSS/IMU in intermediate and terminal guidance stages.

Semi-active laser quadrant detector may provide an accurate line of sight in body axes during last stages of flight. Line of sight vector both in working and earth axes, ($\overrightarrow{X_{p_w}}$) and ($\overrightarrow{X_{p_e}}$) respectively, can be obtained from a hybridized GNSS/IMU and semi-active laser kit set of sensors, using implicitly the calculated rotation matrix to make the transformation. The hybridization algorithm to be used is explained next.

DOI: 10.13009/EUCASS2019-536

Hybridization Algorithm

In order to obtain more accurate results a hybridization process is implemented by mixing the measurements from quadrant detector and the measurements form IMU/GNSS.

The expressions in 17, 18 and the recursive algorithm in 19 and 20 provide the desired solution ($\overrightarrow{M_{sol}}$), where $\overrightarrow{M_{GNSS/IMU}}$ are the measurements obtained by GNSS/INS hybrid sensors defined by vector defined on equation 16, with DCM_{bw} as the director cosine matrix between body and working axes. $\overrightarrow{M_c}$ are the measurements obtained after interpolation by quadrant detector, previously explained and Q and R are experimental covariance matrices for the GNSS/IMU and quadrant detector sensors respectively:

$$\begin{aligned}\overrightarrow{X_{p_{bGNSS/IMU}}} &= DCM_{bw} \cdot \overrightarrow{X_{p_{wGNSS/IMU}}} = \\ &= [x_{p_{bGNSS/IMU}}, y_{p_{bGNSS/IMU}}, z_{p_{bGNSS/IMU}}]\end{aligned} \tag{16}$$

$$\overrightarrow{M_{GNSS/IMU}} = \left\{ \frac{y_{p_{bGNSS/IMU}}}{x_{p_{bGNSS/IMU}}} d_{pCG}, \frac{z_{p_{bGNSS/IMU}}}{x_{p_{bGNSS/IMU}}} d_{pCG} \right\} \tag{17}$$

$$\overrightarrow{M_c} = \{x_c, y_c\} \tag{18}$$

$$\overrightarrow{M_{sol}}\Big|_n = \begin{cases} \overrightarrow{M_{sol}}\Big|_{n-1} + K|_n \left[\overrightarrow{M_{GNSS/IMU}}\Big|_n - \overrightarrow{M_{sol}}\Big|_{n-1} \right] \text{ if } \nexists \overrightarrow{M_c}\Big|_n \\ \overrightarrow{M_{sol}}\Big|_{n-1} + K|_n \left[\overrightarrow{M_c}\Big|_n - \overrightarrow{M_{sol}}\Big|_{n-1} \right] \text{ else} \end{cases} \tag{19}$$

$$K|_n = Q \cdot [Q + R]^{-1} \tag{20}$$

This set of expressions, 17, 18, 19 and 20, represents the procedure to combine and hybridize measurements from GNSS/IMU and quadrant detector in order to obtain a precise line of sight during final stages of flight. The first row in 19 is active when there is not a measurement from quadrant detector, taking the available information only from GNSS/IMU measurements. The second row in 19 is active when there is measurement from quadrant detector and combines measurements from both sensors. Equation 20 takes in account the measurement errors associated with sensors' precision, where Q and R are the error covariance matrix for the GNSS/IMU sensor and for the quadrant photo-detector, respectively.

For a nominal shot, and a typical error on GNSS/IMU sensors of 1 m on each of the three position components, and a random white noise for the quadrant detector of 0.001 on each of the two measurements, and covariance matrices of $Q = 10^{-3} I_{2x2}$ and $R = 10^{-5} I_{2x2}$, where I_{2x2} is the identity matrix of 2 by 2 elements, the results of this hybridizing algorithm are shown in Figure 10. Here, the physical radius of quadrant detector, R_{quad}, has been set to 8 mm.

As it is shown in Figure 10, the GNSS/IMU measurements (black dashed line) degrade in the last stages of flight for both X and Y measurements, while hybrid solution (red dotted line) keeps fidelity to real line of sight (blue continuous line) during the totality of trajectory for both X and Y measurements. As it may be observed, GNSS/IMU measurements are good enough for intermediate guidance but an extra sensor measurement is needed during terminal guidance if precision is required.

After hybridization X_{p_b} vector responds to the following equation 21, which is the composed matrix formed by the hybrid measurements and the panel distance to center of gravity:

$$\overrightarrow{X_{p_b}} = \frac{\left[d_{pCG}, \overrightarrow{M_{sol}}\Big|_n \right]}{\sqrt{d_{pCG}^2 + \left\| \overrightarrow{M_{sol}}\Big|_n \right\|}} \tag{21}$$

3.2 Guidance Law

Guidance is provided in two phases. The first one consists of a constant angle glide trajectory, while the second one consists of a modified proportional law.

3.2.1 Constant Angle Glide

The proposed constant angle glide guidance aims at aligning longitudinal rocket axis (x_b) with a vertical flight plane, which is defined as perpendicular to ground, parallel to the line joining the rocket center of mass and the target, and containing the rocket center of mass. This strategy is elected in order to maximize projectile range. This phase of the trajectory is governed by the following equations: equation 22 which represents the vector between the center

DOI: 10.13009/EUCASS2019-536

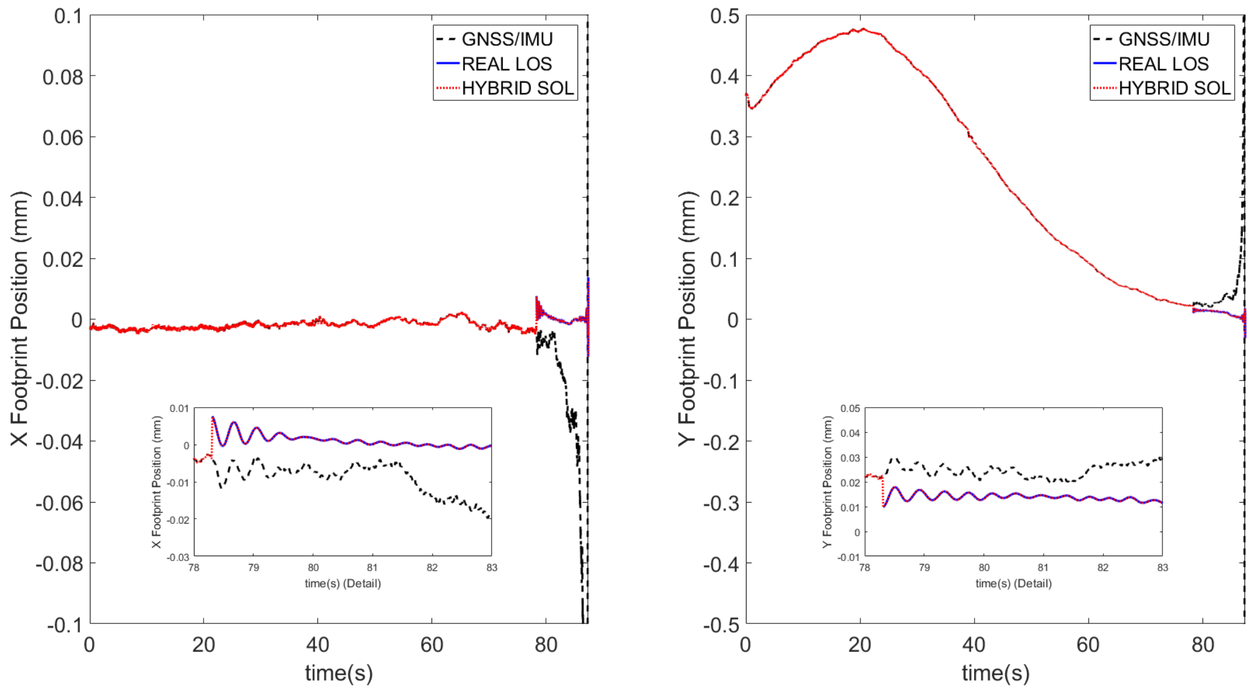

Figure 10: Results for hybridization algorithm.

of mass of the rocket and the target ($\overrightarrow{X_{p_w}}$), also called line of sight, and which is expressed in working axes by its three components ($[x_{p_w}, y_{p_w}, z_{p_w}]$); equation 23 which expresses x_b in working axes ($\overrightarrow{x_{b_w}}$) by its three components ($[x_{b1_w}, x_{b2_w}, x_{b3_w}]$); equation 24 which represents lateral correction or yaw error (ψ_{err}) that needs to be executed to align with the vertical plane defined above; and equation 25 which represents correction in the vertical plane or pitch error (θ_{err}) with respect to a constant glide angle trajectory given by C_1.

Equation 26 means that constant angle glide guidance is only activated when the rocket is after apogee, which is determined by the pitch angle (θ), and flight time is long enough so as to thrust be off. GA_{Act} is a binary variable which is one if guidance is active.

$$\overrightarrow{X_{p_w}} = DCM_{bw}^T \cdot \overrightarrow{X_{p_b}} = [x_{p_w}, y_{p_w}, z_{p_w}] \tag{22}$$

$$\overrightarrow{x_{b_w}} = [x_{b1_w}, x_{b2_w}, x_{b3_w}] \tag{23}$$

$$\psi_{err} = GA_{Act}(atan\frac{z_{p_w}}{x_{p_w}} - atan\frac{x_{b3_w}}{x_{b1_w}}) \tag{24}$$

$$\theta_{err} = GA_{Act}C_1 \tag{25}$$

$$GA_{Act} = \begin{cases} 1 \text{ if } t > 5 \text{ and } \theta \leq 0 \\ 0 \text{ else} \end{cases} \tag{26}$$

3.2.2 Modified Proportional Law

The second phase of guidance consists of a modified proportional law, governed by the following equations: equation 27 gives the yaw error; equation 28 determines the pitch error; equation 29 estimates time to impact (t_{go}); 30 determines the line of sight expressed in earth axes ($\overrightarrow{X_{p_e}} = [x_{p_e}, y_{p_e}, z_{p_e}]$); and 31 states that guidance is only activated when the rocket-target vector vertical component is higher than a given constant (C_2), which involves the last part of the trajectory:

$$\psi_{err} = PN_{Act}\frac{\overrightarrow{X_{p_w}} - \overrightarrow{v_w}t_{go}}{t_{go}^2} \cdot [0, 0, 1] \tag{27}$$

DOI: 10.13009/EUCASS2019-536

$$\theta_{err} = -PN_{Act}\frac{\overrightarrow{X_{p_w}} - \overrightarrow{v_w}t_{go}}{t_{go}^2} \cdot [1,0,0] \tag{28}$$

$$\begin{aligned} t_{go} = max\Bigg[& \frac{1}{g}\left(\overrightarrow{v_w}\cdot[0,1,0] + \sqrt{(\overrightarrow{v_w}\cdot[0,1,0])^2 + 2gy_{p_w}}\right), \\ & , \frac{1}{g}\left(\overrightarrow{v_w}\cdot[0,1,0] - \sqrt{(\overrightarrow{v_w}\cdot[0,1,0])^2 + 2gy_{p_w}}\right)\Bigg] \end{aligned} \tag{29}$$

$$\overrightarrow{X_{p_e}} = \overrightarrow{X_{target_e}} - \overrightarrow{X_e} = [x_{p_e}, y_{p_e}, z_{p_e}], \tag{30}$$

$$PN_{Act} = \begin{cases} 1 \text{ if } atan\frac{z_{pe}}{\sqrt{x_{pe}^2+y_{pe}^2}} \leq C_2 \\ 0 \text{ else} \end{cases} \tag{31}$$

where PN_{Act} is a binary variable which is one if guidance is active, $\overrightarrow{v_w}$ is rocket speed vector expressed in working axes and g is the gravity constant.

3.3 Control System

Here, a novel control law is introduced, which obtains as result two control parameters to be introduced in the actuation system. Control is processed by a double loop feedback system, which uses accelerations and angular speeds in body axes. The inner loop is only used as a system of stability augmentation. The two control parameters are the control angle for the rotating force (ϕ_c) and the module of the control force (τ_c).

The control angle for the rotating force (ϕ_c) is defined in equation 32, taking pitch (θ_{err}) and yaw (ψ_{err}) errors as inputs. The module of the control force produced (τ_c) is also controlled. It is calculated as in equation 33; note that this is done by processing the quadratic average of pitch and yaw errors. Equation 34, computes when the guidance, navigation and control system is activated (GNC_{Act}). In this expressions $L1$ and $L2$ are experimental gains in order to tune the errors, K_i, K_d and K_p are the integral, derivative and proportional constants of a controller, and K_{mod} is a constant in order to adjust force module.

Figure 11 shows the philosophy of the controller. It has three main inputs: the acceleration of the rocket in body axes, expressed by its three components $[acc_{xb}, acc_{yb}, acc_{zb}]$, the pitch error and yaw errors and the measurements from gyros on each axis, $[\phi, \theta, \psi]$. Roughly speaking, the controller calculates the needed pointing angle of the aerodynamic force calculating the arc-tangent of the quotient of the pitch and yaw error. This gives an angle at which the aerodynamic force, in the $y_b - z_b$ plane, must point to reach the target. However, the gyroscopic effect due to the spinning part of the rocket makes the response difficult to govern, i.e., imposing a ϕ_c of 90 degrees will not make the rocket to respond upwards. Therefore, we also need to measure the acceleration of the rocket, without accounting for gravity, and make the difference between the angle that forms the projection of the aerodynamic force in the $y_b - z_b$ plane with y_b and ϕ_c zero.[3]

$$\begin{aligned} \phi_c = GNC_{Act}\Bigg\{ & K_p\left[atan\frac{\theta_{err}-L_1\theta}{L_2(\psi_{err}-L_1\psi)} - atan\frac{acc_{zb}}{acc_{yb}}\right] + \\ & +K_i\int\left[atan\frac{\theta_{err}-L_1\theta}{L_2(\psi_{err}-L_1\psi)} - atan\frac{acc_{zb}}{acc_{yb}}\right]dt + \\ & +K_d\frac{d}{dt}\left[atan\frac{\theta_{err}-L_1\theta}{L_2(\psi_{err}-L_1\psi)} - atan\frac{acc_{zb}}{acc_{yb}}\right] + atan\frac{\theta_{err}-L_1\theta}{L_2(\psi_{err}-L_1\psi)}\Bigg\} \end{aligned} \tag{32}$$

$$\tau_c = GNC_{Act}K_{mod}\sqrt{(\theta_{err} - L_1\theta)^2 + (L_2(\psi_{err} - L_1\psi))^2} \tag{33}$$

$$GNC_{Act} = GA_{Act} \vee PN_{Act} \tag{34}$$

In order to translate these control parameters into fin deflections, i.e., $\delta_1, \delta_2, \delta_3$ and δ_4, managed by two actuators, the following relationships are applied:

$$\delta_1 = \delta_3 = \tau_c sin\phi_c \tag{35}$$

$$\delta_2 = \delta_4 = \tau_c cos\phi_c \tag{36}$$

DOI: 10.13009/EUCASS2019-536

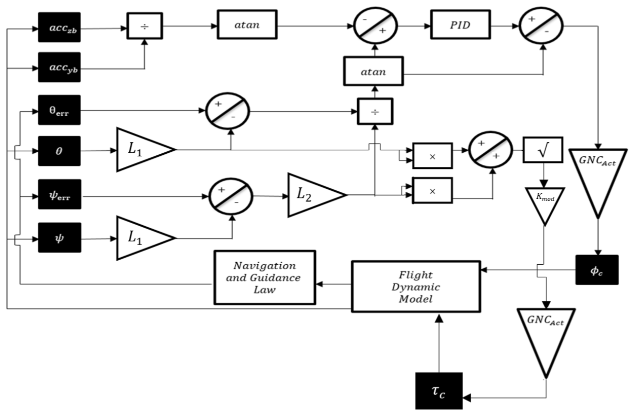

Figure 11: Control system scheme.

4. Numerical Simulations

Simulation results are presented using the nonlinear flight dynamics model[3] in order to demonstrate closed-loop performance of the presented navigation, guidance and control novel approach and contrast performance with ballistic flight and GNSS/IMU controlled flight. MATLAB/Simulink R2016a on a desktop computer with a processor of 2.8 Ghz and 8 GB RAM was used.

The rest of this section is divided in two different subsections. The first one presents the ballistic flights of the nominal trajectories to which the navigation, guidance and control algorithms developed will be applied. The second one performs Monte Carlo simulations so as to compare ballistic flights, controlled flights with GNSS/IMU guided trajectory and controlled flights with GNSS/IMU/SALK guidance. Also, an ideal controller with no errors introduced in the line of sight is used in order to compare with ideal results of guidance.

4.1 Nominal Trajectories

To test the algorithms developed, three nominal trajectories will be employed, which differ in their launch or initial picth angle: 20°, 30° and 45°. Table 3 shows the characteristic parameters for these shots: initial pitch angle in the first column, initial lateral correction in the second one, and impact point in the last one. Initial lateral correction is performed in order to compensate Coriolis and gyroscopic forces as it is showed in.[3]

Initial Pitch Angle (°)	Initial Lateral Correction (°)	Impact point (m)
20	0.1524	18790.38
30	0.1989	23007.26
45	0.3082	26979.00

Table 3: Nominal trajectories' parameters.

4.2 Monte Carlo Simulations

Monte Carlo analysis is conducted to determine closed-loop performance across a full spectrum of uncertainty in initial conditions, sensor data acquisition (as it was expressed on covariance matrix for sensors), atmospheric conditions, and thrust properties. For atmospheric conditions variations in turbulence are considered using the specification MIL-F-8785C and the Dryden Wind turbulence model. Monte-Carlo simulation distribution parameters are listed in Table 4. A set of 2000 shots is performed for each of the following combinations: ballistic shots, GNSS/IMU assisted shots, GNSS/IMU/SALK assisted shots and ideal controller assisted shots. The ideal controller is the result of taking the real line of sight independently from measurements. Initial shot angles of 20°, 30° and 45° are performed. Note that a total of 24000 simulations are performed at the end of simulation campaign.

DOI: 10.13009/EUCASS2019-536

Parameter (deg)	Mean	Standard Deviation
Initial ϕ	0°	20°
Initial Pitch	Nominal (20°, 30°, 45°)	0.01°
Wind Speed	10 m/s	5 m/s
Wind Direction	0°	20°
Thrust at each time instant	T(t)	10 N
Initial azimuth deviation	Nominal lat. correction	0.01°

Table 4: Monte carlo simulation parameters.

4.3 Discussion

The results for the ballistic trajectories for the three proposed initial pitch angles are shown in Figure 12. It shows impact point dispersion patterns for each of the ballistic cases. Also, the circular error probable (CEP) may be observed for each of the initial shot pitch angle.

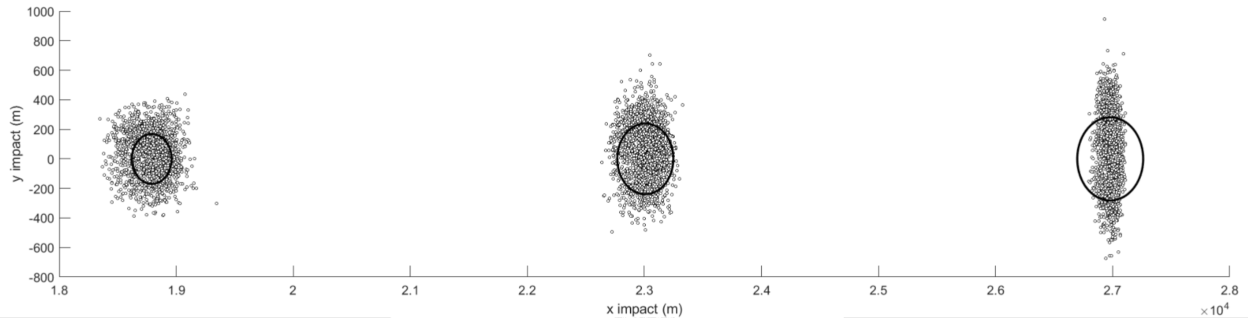

Figure 12: Ballistic shots for 20°, 30° and 45° initial pitch angles.

Values for navigation, guidance and control parameters defined on previous sections (C_1, C_2, K_i, K_p, K_d, K_{mod}, L_1 and L_2) are expressed on table 5. These parameters where selected experimentally in the model in order to obtain stable flight conditions. Note that values for K_i, K_p, K_d, and L_2 differs from controlled flight phase 1 and 2 because the different nature of flight conditions present on each phase.

Parameter	C_1	C_2	K_i	K_p	K_d	K_{mod}	L_1	L_2
Value for phase 1	-7.5 deg	-21 deg	0	0.5	0	0.08	0.01	100
Value for phase 2	-7.5 deg	-21 deg	1	0.25	0.05	0.08	0.01	1

Table 5: Values for the constants on each flight phase.

Figure 13 shows detailed information about comparisons between different approaches. On the left ballistic flights and GNSS/IMU assisted flights are compared, on the middle-left GNSS/IMU and GNSS/IMU/SAL assisted flights, on the middle-right GNSS/IMU/SAL and ideal controller assisted flights, and finally on the right ballistic flights and GNSS/IMU/SAL assisted flights. Note that the ideal controller works with an ideal line of sight which is defined here as the result of calculating the real vector between center of mass of the rocket and target, without introducing any error in the process. But using this ideal line of sight there is still an error which is associated with the aerodynamic response of the rocket. The controlled flights exhibit tighter impact groupings, getting tither for the GNSS/IMU/SALK and Ideal controllers. Spread in the impact distribution does remain in the guided flights with GNSS/IMU controller due to the difficulties discussed before. Note that improvements or reductions on the CEP of a 95% are obtained.

The circular error probable (CEP) for each of the targets and for ballistic and controlled flights are shown in Table 6.

5. Conclusions

A novel approach, which is based on an innovative hybridization between GNSS/IMU and semi-active laser quadrant photo-detectors, has been developed.

Throughout this paper we have presented several strategies to improve the guidance, navigation and control of a highly spinning rocket controlled with the output of GNSS/IMU sensors. The control of this rocket is performed by

DOI: 10.13009/EUCASS2019-536

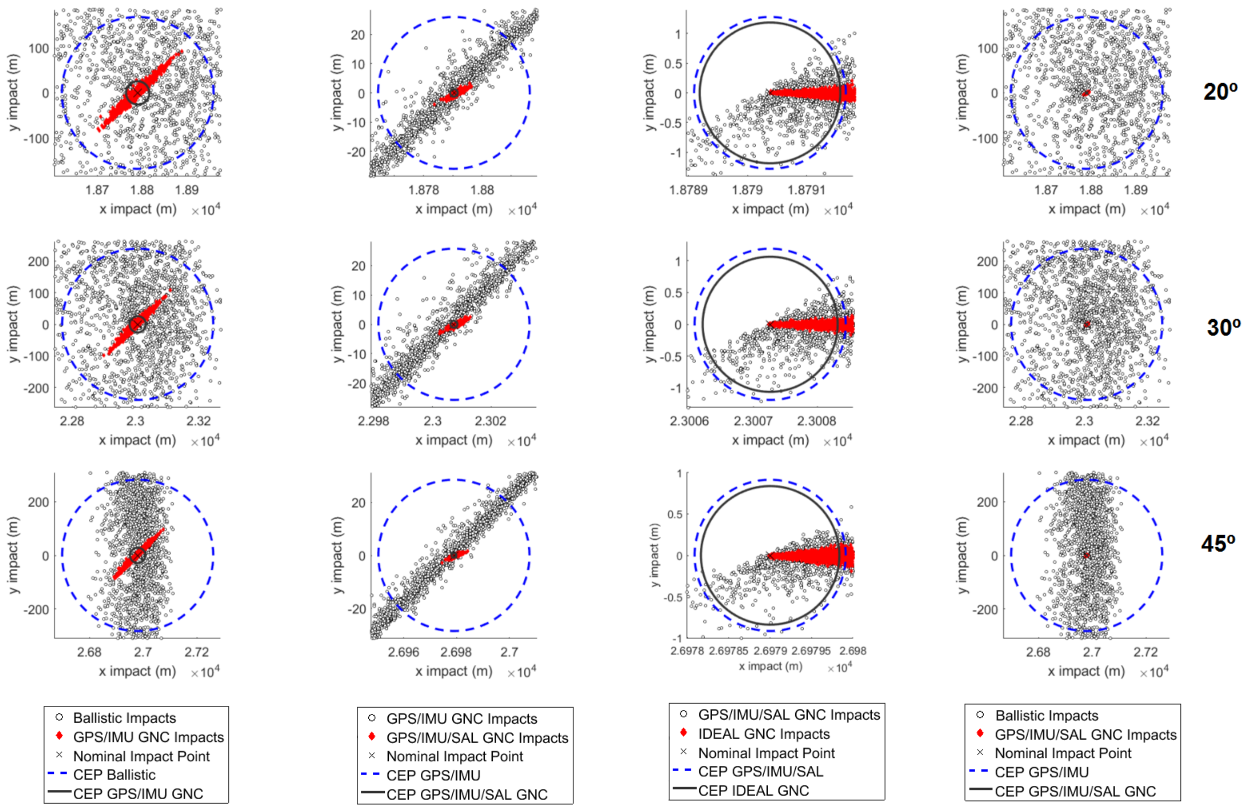

Figure 13: Detailed shots for different algorithms.

Nominal Pitch (deg)	Ballistic Flight (m)	GNSS/IMU Controlled Flight (m)	GNSS/IMU/SALK Controlled Flight (m)	Ideal Controlled Flight (m)
20	169.34	25.97	1.28	1.18
30	239.37	25.77	1.18	1.06
45	281.59	28.61	0.91	0.83

Table 6: Circle error probable in different cases.

DOI: 10.13009/EUCASS2019-536

means of an actuator placed at its head with four fins coupled two by two.

First, a flight dynamics model has been introduced and detailed for both the rocket and actuator. We focused specially in the non-linear dynamics of the problem, providing aerodynamic coefficients that are Mach number dependent, variating for each flight step.

By means of this model, we find out that small errors of around 1 m in GNSS/IMU systems induce giant errors in line of sight vector calculation. The reason for this behavior is that small errors within small distances between rocket center of mass and target produce high angular errors in line of sight.

Consequently, we proposed an approach that hybridize the outputs of the aforementioned sensors and one from a low-cost semi active laser quadrant photo-detector. This methodology can improve the precision of line of sight determination during the terminal guidance of artillery rockets, and therefore the precision on impact point. In addition to this, we introduced a two-phase guidance algorithm and a novel control technique for high-rate spinning rockets. The guidance algorithm is based on a constant angle glide and on a modified proportional law while the control algorithm is based on a simple but effective and robust double-input double-output controller.

The proposed algorithms improve accuracy in an order of magnitude (from 20 m to around 1) by mixing those inaccurate signals in the terminal trajectory, with the signals of a precise semi-active laser quadrant detector, which can determine line of sight with high fidelity in body axes. Using the proposed hybridized algorithm during the last phases of flight, improves accuracy nearly to the ideal case as it was proved in simulations.

References

[1] A. Budiyono and H. Rachman. Proportional guidance and cdm control synthesis for a short-range homing surface-to-air missile. *Journal of Aerospace Engineering*, 25(2):168–177, 2012.

[2] R.d. Celis and L. Cadarso. Spot-centroid determination algorithms in semiactive laser photodiodes for artillery applications. *Journal of Sensors*, 2019.

[3] R.d. Celis, L. Cadarso, and J. Sánchez. Guidance and control for high dynamic rotating artillery rockets. *Aerospace Science and Technology*, 64:204–212, 2017.

[4] M. A. Creagh and D. J. Mee. Attitude guidance for spinning vehicles with independent pitch and yaw control. *Journal of guidance, control, and dynamics*, 33(3):915–922, 2010.

[5] F. Fresconi and J. Rogers. Flight control of a small-diameter spin-stabilized projectile using imager feedback. *Journal of Guidance, Control, and Dynamics*, 38(2):181–191, 2015.

[6] R. Hamilton. Precision guided munitions and the new era of warfare. *Air Power Studies Centre, Royal Australian Air Force.*, https://fas.org/man/dod-101/sys/smart/docs/paper53.htm, 1995.

[7] K. Holldack, W.B. Peatman, and T. Schroeter. Vertical photon beam position measurement at bending magnets using lateral diodes. *Review of scientific instruments*, 66(2):1889–1891, 1995.

[8] N. Lechevin and C.A. Rabbath. Robust discrete-time proportional-derivative navigation guidance. *Journal of Guidance, Control, and Dynamics*, 35(3):1007–1013, 2012.

[9] K. Li, S. Yang, and L. Zhao. Stability of spinning missiles with an acceleration autopilot. *Journal of Guidance, Control, and Dynamics*, 35(3):774–786, 2012.

[10] P.S. Maybeck, T.D. Herrera, and R.J. Evans. Target tracking using infrared measurements and laser illumination. *IEEE transactions on aerospace and electronic systems*, 30(3):758–768, 1994.

[11] P. Torrey S. Kohli S. Snyder, L. Tellman. Ins/gps operational concept demonstration (ocd) high gear program. *IEEE Aerospace and Electronic Systems Magazine*, 9(8):38–44, 1994.

[12] G. Schmidt and R. Phillips. Ins/gps integration architecture performance comparisons. In *NATO RTO lecture series: Low-cost Navigation sensors and integration technology*, volume RTO-EN-SET-116. 2011.

[13] S. Theodoulis, V. Gassmann, P. Wernert, L. Dritsas, I. Kitsios, and A. Tzes. Guidance and control design for a class of spin-stabilized fin-controlled projectiles. *Journal of Guidance, Control, and Dynamics*, 36(2):517–531, 2013.

[14] E. L. Waltz and D. M. Buede. Data fusion and decision support for command and control. *IEEE Transactions on Systems, Man, and Cybernetics*, 6(12):865–879, 1986.